Journal of Physics and Chemistry of Solids 167 (2022) 110775

Contents lists available at ScienceDirect

Journal of Physics and Chemistry of Solids

journal homepage: www.elsevier.com/locate/jpcs

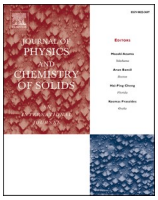

Mechanochemically induced solid-state CO_2 capture during the synthesis of SnO_2 nanoparticles

Gábor Kozma [a,*], Andrea Rónavári [a], Zoltán Kónya [a,b], Ákos Kukovecz [a]

[a] Department of Applied and Environmental Chemistry, University of Szeged, Hungary
[b] MTA-SZTE Reaction Kinetics and Surface Chemistry Research Group, Hungary

ARTICLE INFO

Keywords:
CO_2 capture
Mechanochemistry
Sodium bicarbonate

ABSTRACT

Mechanochemistry offers a versatile method to synthesize metal oxides by the reaction of the corresponding metal salt and Na_2CO_3, with CO_2 as a by-product. It is possible to monitor the progress of the reaction and even calculate conversion values based on the measured pressure increase in the milling equipment. We studied the kinetics of tin oxide formation in the mechanochemical reaction between $SnCl_2$ and Na_2CO_3. Our systematic experiments revealed unexpected complexity in the temporal pressure function depending on the exact composition of the reactant mixture: the pressure exhibited a clear local maximum, and pressure values even dropped close to their starting value by the end of the reaction when Na_2CO_3 was present in 100% excess. This anomaly can be explained by realizing that CO_2 is captured as $NaHCO_3$ in a process analogous with aqueous flue gas treatment, and it can also be released in the secondary reaction between unreacted $SnCl_2$ and $NaHCO_3$. Here we provide experimental evidence to support this hypothesis and to draw attention to the pitfalls of over-simplifying pressure-based conversion calculations in mechanochemical processing.

1. Introduction

Mechanochemistry is a widely used solid-phase synthesis approach. It is particularly well-suited for the production of metal oxide nanoparticles [1,2] by utilizing the reaction of a metal salt and sodium carbonate. For example, this method has been successfully applied to produce lead-free [3] or niobate-containing ceramics [4], and Intasa-ard et al. presented the mechanochemical preparation of layered double hydroxides in a comprehensive study using Na_2CO_3 in many cases [5]. The most typical mechanochemical uses of sodium carbonate are in the production of metal oxide photocatalysts [6], spinel oxide [7], or nanofluid [8] components.

During these reactions, CO_2 is generated, resulting in a pressure increase in the milling drum. In fact, pressure changes during any mechanochemical reaction offer valuable insight into the kinetics of the process. Borchard et al. monitored pressure during the synthesis of nitrogen-doped porous carbon. They detected a sudden rise in pressure and associated it with the instantaneous formation of carbon [9]. The probe can also be used in reactive gas syntheses: Castro et al. measured the pressure of H_2 during grinding and explained the observed pressure decrease by H_2 consumption in the closed milling vessel [10]. In the synthesis of MgH_2 by Gutfleisch et al., reaction progress monitoring was based on measuring the decrease in H_2 pressure [11]. During high-energy milling of iron oxide, an increase and then a decrease in pressure were observed by Gheisari et al. The former was related to released oxygen, whereas the pressure drop was allocated to the reaction of vacant iron oxide, oxygen, and iron [12]. Similar results were obtained in the case of reactive milling of Bi_2O_3–Fe by Hasanpour et al. [13] Even in cases without chemical reaction between the gas and the reactants during milling, the possibility of a change in pressure must be taken into account. Coste et al. observed a gradual decrease in pressure while TiO_2 and Al_2O_3 were co-milled and they explained it by adsorption of oxygen on the new surfaces formed during the process [14]. Gamrat et al. ground a $Cu_2(OH)_2CO_3$–Al composite; during the reaction, $Cu_2(OH)_2CO_3$ decomposed to CuO with release of CO_2 and H_2O, which caused a significant increase in pressure in the milling drum [15].

Numerous instruments are available for mapping reaction pathways, reaction mechanisms, and kinetics [16–21]. One of these devices is the GTM-II gas pressure and temperature measuring system produced by Fritsch GmbH, Germany [22,23], which allows simultaneous in situ measurement of pressure and temperature in the atmosphere of the milling bowl. The lid of the bowl is equipped with a radio transmitter

* Corresponding author.
E-mail address: kozmag@chem.u-szeged.hu (G. Kozma).

https://doi.org/10.1016/j.jpcs.2022.110775
Received 3 January 2022; Received in revised form 29 April 2022; Accepted 30 April 2022
Available online 5 May 2022

that sends data continuously to the computerized receiver unit, thereby providing real-time information about the reaction kinetics. Although the practicality of the GTM instrument is unquestionable, it is important to correctly interpret the data it provides as we show.

The mechanochemical model reaction of choice in our group is the synthesis of tin oxide nanoparticles. Tin(IV) oxide (SnO_2) is a well-known semiconductor material [24,25], and widely used such as a gas sensor [26–29], in batteries [30–32] and solar cells [33–35], and as a catalyst in pure or composite form [36–38]. One of the most straightforward and high-yielding methods for producing nanoscale SnO_2 is the mechanochemical synthesis [39,40]. The aforementioned CO_2 generation has been observed in the process [41] in which $SnCl_2$ reacts with Na_2CO_3 according to Eq. (1):

$$SnCl_2 \cdot 2H_2O + Na_2CO_3 \rightarrow SnO + 2NaCl + CO_2 + 2H_2O \quad (1)$$

Further treatment by calcination at 600 °C in air atmosphere for 2 h results in SnO_2 (Eq. (2)):

$$SnO + \frac{1}{2}O_2 \rightarrow SnO_2 \quad (2)$$

Reaction (1) is second-order, therefore, a saturation type CO_2 pressure vs time curve is anticipated, where the plateau would indicate completion of the process. However, performing the actual experiment revealed markedly different behavior. Moreover, the presence of excess Na_2CO_3 transformed the curve into one with a clear pressure maximum. Having reached the maximum, the pressure gradually dropped back to a level determined by the quantitative excess of sodium carbonate. In this report we offer an explanation for this anomalous behavior by suggesting that the formed CO_2 is re-captured at the later milling stages in the form of $NaHCO_3$.

2. Experimental

2.1. Ball-milling experiments

Ball-milling experiments were performed in a Fritsch Pulverisette-6 planetary ball mill equipped with a GTM-II in-line temperature and pressure monitoring system. Each experiment was performed at room temperature in air atmosphere in a 250-mL stainless-steel drum containing 50 stainless-steel balls of 10 mm in diameter. The parameters are shown in Table 1.

The drum was filled with a mixture of $SnCl_2{\cdot}2H_2O$ and Na_2CO_3, along with NaCl as a reaction matrix. The composition of the mixture varied to achieve 100% stoichiometric Na_2CO_3 excess with respect to Eq. (1). in 10% steps (Table 2).

The NaCl matrix was used to prevent the aggregation of the reactant and product materials, and to set the total weight of the mixtures to the same value (30 ± 0.01 g) in each experiment [42]. The NaCl is an ideal matrix material because it is also a reaction product according to Eq. (1), therefore, it does not alter the chemical environment of the process. In addition, the use of NaCl crystals as a grinding matrix plays a role in providing a large surface area for calcination, thereby inhibiting the merging of individual particles. The produced tin oxide nanoparticles were calcined at 600 °C in air. Byproducts and unreacted precursors were subsequently removed by washing with distilled water. Finally, the product was centrifuged and dried at 60 °C in air overnight.

Table 1
Parameters used in the milling process. GV, grinding vial; GB, grinding ball.

Parameter	Value
Duration of grinding	4 h
Rotational speed	300/500 rpm
Type of GV and GB	Fe–Cr (X105CrMo17)
Volume of GV	260 mL
Diameter of GV (internal)	80 mm
Number of GB	50 pieces
Weight of GB	4 g
Diameter of GB	10 mm
Transmission ratio	−1.82

Table 2
Composition of each sample.

Sample	Na_2CO_3 excess	$SnCl_2{\cdot}2H_2O$ (g)	Na_2CO_3 (g)	NaCl (g)
A	0%	6.38	3.0	20.62
B	10%		3.3	20.32
C	20%		3.6	20.02
D	30%		3.9	19.72
E	40%		4.2	19.42
F	50%		4.5	19.12
G	60%		4.8	18.82
H	70%		5.1	18.52
I	80%		5.4	18.22
J	90%		5.7	17.92
K	100%		6.0	17.62

2.2. Definition of CO_2 conversion

The pressure was measured continuously while using the GTM-II unit. The CO_2 conversion percentage (K) was calculated as follows:

$$K(\%) = \left[\frac{[p_{GTM} - p_0] \times [V_v - (V_b + V_m)]}{R \times T_{GTM}}\right] \Big/ [n_{CO_2} * 100] \quad (3)$$

where p_{GTM} is the actual pressure measured by the GTM-II head during the reaction, p_0 is atmospheric pressure, V_v is volume of the vial, V_b is total volume of the balls, V_m is volume of the admeasured materials, R is the universal gas constant, T_{GTM} is actual temperature measured by the GTM-II head, and n_{CO2} is the total amount of CO_2 generated in the reaction calculated from the amount of Na_2CO_3 in the reaction. The amount of CO_2 at a given time can be calculated from p_{GTM}. The free volume of the vial (221.65 cm^3) was calculated from the loading and density data by correcting the total drum volume (260.03 cm^3) for the volume of the grinding balls and admeasured materials. The volume of the 50 balls was 26.18 cm^3, and the average volume of the solid materials was 12.2 cm^3.

2.3. Characterization

Powder X-ray diffractogram (XRD) patterns were recorded using a Rigaku Miniflex 2 unit equipped with a Cu Kα radiation source (4°/min resolution, 2θ = 4–80°). Fourier transform infrared spectroscopy (FT-IR) studies were carried out using a Bruker Vertex 70 instrument (16 scans/s, 4 cm^{-1} resolution) using the KBr pellet technique. Thermogravimetry–differential thermogravimetry (TG–dTG) measurements were conducted using a Setaram Labsys instrument (5 °C/min, N_2 atmosphere, 25–1000 °C).

3. Results and discussion

The theoretical and recorded pressure curves are shown in Fig. 1 for sample A (stoichiometric reaction mixture). The expected maximum pressure was calculated from the admeasured Na_2CO_3 quantity. Assuming complete transformation of the reactants, the calculated maximum pressure should have been 425 kPa. However, at the end of the experiment (after 60 min), the measured temperature was 31 °C and the final measured pressure was 388 kPa. This difference indicates that the conversion was 91.3%. The course of the curve will be discussed in detail later, but for the sake of interpretation, the division of the dominant reaction paths is presented here. The total pressure–time curve was divided according to the dominant reaction pathways (A–D). In stage A, reaction as per Eq. (1) is decisive, i.e. transformation of starting materials into products. This is followed by stage B, where the

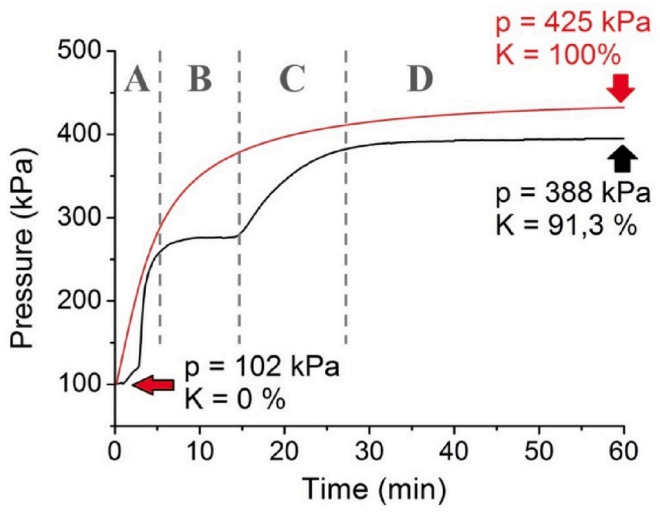

Fig. 1. The theoretical (red) and the GTM-recorded (black) pressure (p) as a function of time for sample A (K, conversion rate). Parts are the division of the entire process by the dominant reaction path: A (Eq. (1)), B (Eq. (1)) = (Eq. (4)), C (Eq. (5)), D (Eq. (1)).

reaction paths Eq. (1) and Eq. (4) are in quasi-equilibrium. In stage C, product formation again prevails based on reaction as per Eq. (5), which is again replaced by reaction as per Eq. (1) due to decomposition of $NaHCO_3$ in stage D, which leads to the depletion of the starting materials.

This example illustrates how pressure curves are typically interpreted in routine mechanochemical laboratory practice. However, this simple approach has certain pitfalls that can be avoided by understanding the CO_2 chemistry of the system. First, there is a profound difference between the shapes of the measured and calculated pressure curves. At the beginning of the experiment, a slow increase in pressure was observed rather than the steep rise suggested by the calculated curve. This discrepancy can be explained by the initial inhomogeneity of the reactant materials, which slowed the reaction. However, 2–3 min of ball-milling was sufficient for the reaction mixture to reach a well-homogenized state. At this point, the precursor materials could react over a large surface area, which led to a rapid increase in the reaction rate. Because the reactions are second-order, the reaction rate should gradually decrease, eventually reaching a plateau when no more reactants are available in the mixture (indicated by plateauing pressure in the calculated curve). Instead, the measured curve suggested a two-step reaction profile. The initial marked increase of pressure after ~3 min plateaued rapidly after the 5 min and remained constant until 15 min. After 15 min ($p \cong 280$ kPa), a secondary chemical reaction was initiated, as indicated by an increase in pressure, which then gradually reached its maximum value. No significant changes were observed after 30 min (The actual milling processes was continued for an additional 3 h; however, since no additional changes were observed, this part of the curves is not shown.)

To further investigate the unexpected two-step profile of the measured curve for sample A, a series of experiments with increasing Na_2CO_3 content were performed. In all experiments the mill speed was set to 500 rpm, whereas the other parameters remained the same as those used for sample A. The results are shown in Fig. 2a.

Increasing the amount of Na_2CO_3 profoundly affected the shape of the pressure curves (Fig. 2a). In samples B–F, the corresponding plateau observed at around 10–15 min in the curve for sample A gradually became a downward slope, while the final pressure after the second pressure increase step (at approximately 30–40 min in sample A) also decreased continuously. As the Na_2CO_3 surplus was further increased in samples G–K, the characteristic two-step shape of the pressure curve gradually disappeared. In order to get a better understanding of the

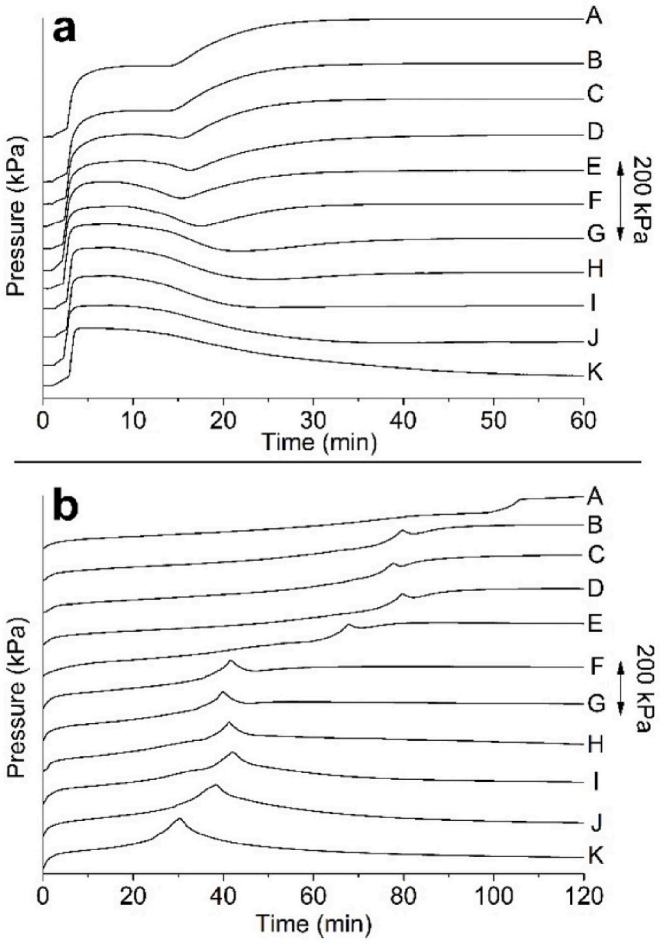

Fig. 2. The pressure vs. time curves recorded at (a) 500 and (b) 300 rpm with increasing Na_2CO_3 surplus (A: +0%, B: +10% … K: +100%). Curves are shifted along the y-axis for better visibility.

processes occurring within the first 30 min of milling, the resolution of the pressure curves was increased by reducing the rotation speed to 300 rpm to expand the critical phase in time (Fig. 2b). This revealed that the first pressure plateau was actually a well-defined peak of the pressure vs. time function.

The final pressure values, the local pressure maxima, and the time required to reach them were extracted from Fig. 2b and shown in Fig. 3.

In the case of sample A (stoichiometric ratio), the measured final pressure was around 400 kPa (Fig. 3a), whereas this value was less than 130 kPa for sample K (100% Na_2CO_3 excess). Thus, on average, the final pressure decreased by 25 kPa per 10 wt% Na_2CO_3 excess. The pressure started to decrease after 290 kPa regardless of the amount of excess Na_2CO_3 (Fig. 3b). This result means K = 57% precursor conversion. This value is equal to the value measured in the plateau region of the curve preceding the second pressure rise in the case of sample A (Fig. 1). In addition, the time needed to reach the local pressure maximum differed, because the more Na_2CO_3 that was added to the reaction mixture, the less time was required to reach this pressure (from 107 min in sample A to 30 min in sample K). Apparently, the driving force for the anomalous pressure curve was related to the excess carbonate ratio. The shift of the local pressure maximum can be explained by the increasing Na_2CO_3 excess in the system, which resulted in a greater probability of $SnCl_2$ and Na_2CO_3 encounters. Thus, the surplus Na_2CO_3 significantly accelerated transformation of the reactants.

The SnO_2 particle morphology was examined using transmission (TEM) and scanning electron microscopy (SEM) images of the completely treated (calcined and washed) samples A and K (Fig. 4). The

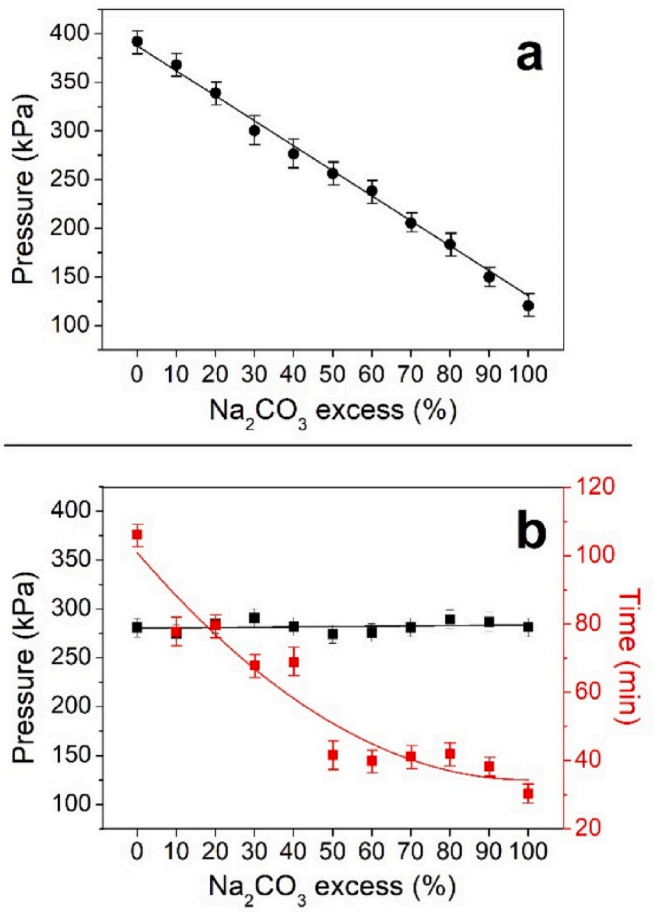

Fig. 3. (a) Final (●) and (b) local pressure maxima (■), and the time required to reach them (■).

images showed no difference in morphology of the nanoparticles. For both samples, the average size of SnO_2 particles was 9 nm, with no significant difference in the diameter distribution. It can be concluded that, from a morphological point of view, the Na_2CO_3 excess did not affect the formation of SnO_2.

The XRD measurements were performed to investigate the effect of excess Na_2CO_3 on the quality of the final product. Fig. 5 shows XRD patterns of the milled, calcined, and washed sample A. Because of the dominant presence of NaCl, only the most intense reflections of SnO_2 were detected in the pattern of the calcined sample at $2\Theta = 26.5^\circ$ (110), 33.8° (101), 37.9° (200), and 51.8° (211). After the sample was thoroughly washed, the characteristic reflections of SnO_2 became visible in the diffractogram. The diffraction patterns of the washed and calcined product of all samples A–K matched within experimental error; therefore, we conclude that the $SnCl_2$ to Na_2CO_3 ratio did not affect quality of

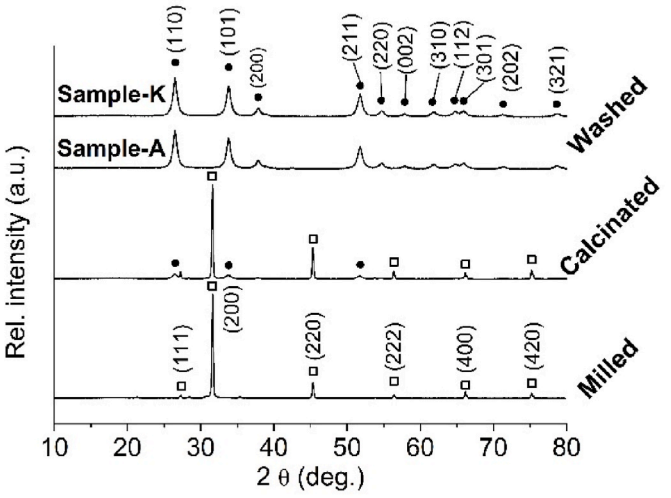

Fig. 5. XRD patterns of the milled, calcined, and completely treated samples A and K (□, NaCl; •, SnO_2).

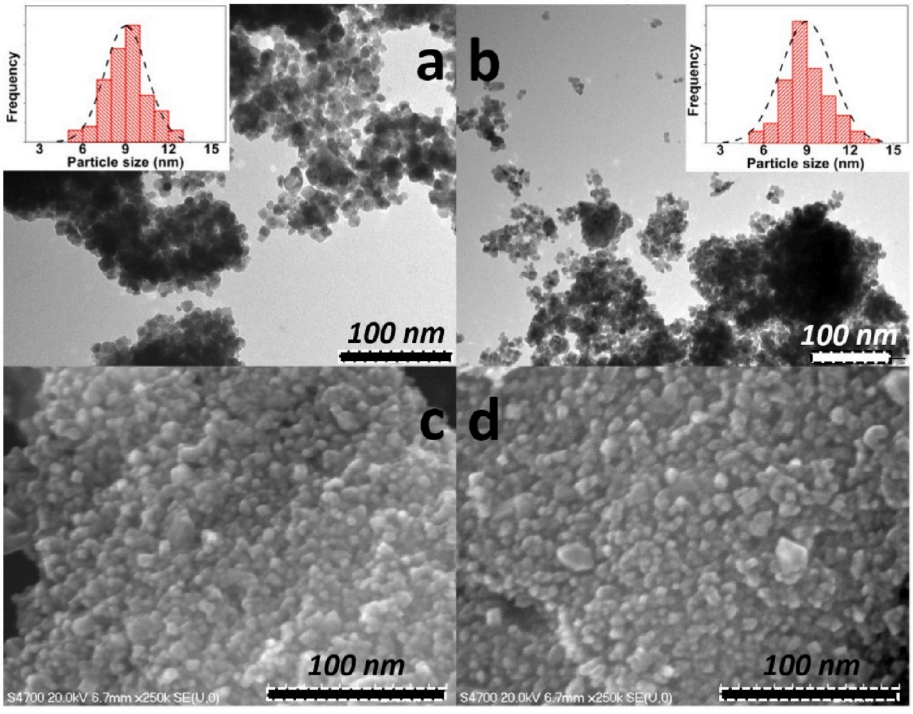

Fig. 4. TEM and SEM images of samples A (a, TEM; c, SEM) and K (b, TEM; d, SEM).

the final SnO_2 product.

Having established the chemical equivalence of the end products derived from samples A–K, it was necessary to investigate the temporal progress of the reactions so that the pronounced differences in the pressure curves could be explained. Fig. 6a and c shows the FT-IR spectra of samples A and K, respectively, as recorded at representative stages of the reaction identified in the corresponding pressure curves (Fig. 6b and d). Large amounts of Na_2CO_3 were detected in sample A after 1 and 20 min of milling, as indicated by peaks at 1445 and 877 cm^{-1}. Peaks representing Sn–O and O–H were shown at 607 and 1622 cm^{-1}, respectively. The peaks corresponding to Na_2CO_3 gradually decreased in intensity with increasing reaction time, whereas the peaks representing the products became more characteristic with increasing reaction time. After 90 min, Na_2CO_3 was no longer detectable. These peaks were identified in a previous study [41]. In the case of sample K (Fig. 6c), as early as after 1 min of milling, characteristic peaks of $NaHCO_3$ appeared, and became more intense as milling progressed. The $NaHCO_3$ was formed (Eq. (4)) as a result of excess Na_2CO_3 reacting with CO_2 and H_2O released in the main tin oxide synthesis reaction.

$$Na_2CO_3 + CO_2 + H_2O \leftrightarrow 2NaHCO_3 \quad (4)$$

This side-reaction consumed some of the CO_2 formed in the main process (Eq. (1)). Through the formation of $NaHCO_3$, CO_2 was continuously captured from the atmosphere of the reaction vessel, therefore, it is safe to assume that this process was responsible for the unexpected pressure decrease.

To confirm the hypothesis that CO_2 is stored as $NaHCO_3$ in this system, TG–dTG measurements were performed (Fig. 7). The end products of the reaction for samples A and K were collected after 120 min of milling, when the samples presumably contained only the final products. In the case of sample A, the slight decrease in mass at the beginning of the process is attributed to desorption (des.) of remaining water in the sample.

As temperature increased to 800 °C, no significant change in mass was observed, then as temperature increased further, evaporation (ev.) of NaCl occurred. In contrast, sample K exhibited a pronounced weight loss as temperature increased to 150 °C. This was the combined effect of water desorption and $NaHCO_3$ decomposition to CO_2, H_2O, and Na_2CO_3.

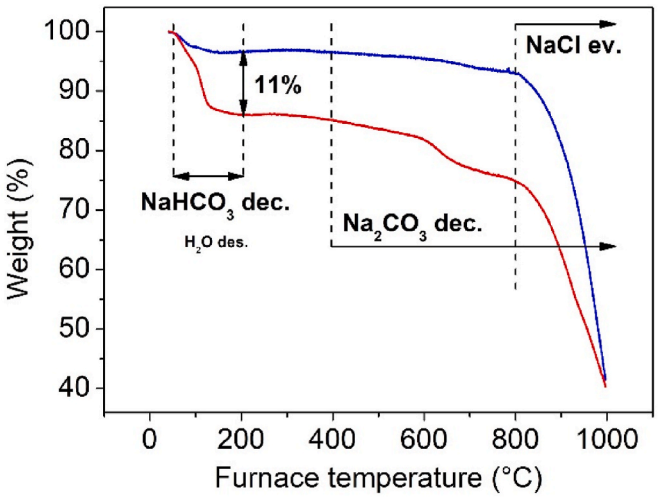

Fig. 7. TG–dTG measurement results of samples A (blue) and K (red).

When the process was completed at 200 °C, the actual weight loss compared to sample A was 11.16%, whereas the theoretical weight loss estimated by assuming stoichiometric $NaHCO_3$ formation and decomposition was 11.7%. The values match within the error of the experiment. This convincingly supports the hypothesis that CO_2 was stored in the form of $NaHCO_3$.

The $NaHCO_3$ was also consumed in its direct reaction with $SnCl_2$ as summarized in Eq. (5). This process releases previously captured CO_2 into the atmosphere as long as unreacted $SnCl_2$ is still available.

$$SnCl_2 \times 2H_2O + 2NaHCO_3 \rightarrow SnO + 2NaCl + 3H_2O + 2CO_2 \quad (5)$$

The presented evidence confirms that CO_2 capture summarized in Eq. (4) was the reason for the unexpected pressure profile of the tin oxide synthesis reaction. The elemental steps of this process are well known and have been described in detail [43]. Crystal water entering the system with the $SnCl_2$ provides the necessary aqueous film phase for the reaction. Firstly, the balance of gaseous and dissolved CO_2 shifts in

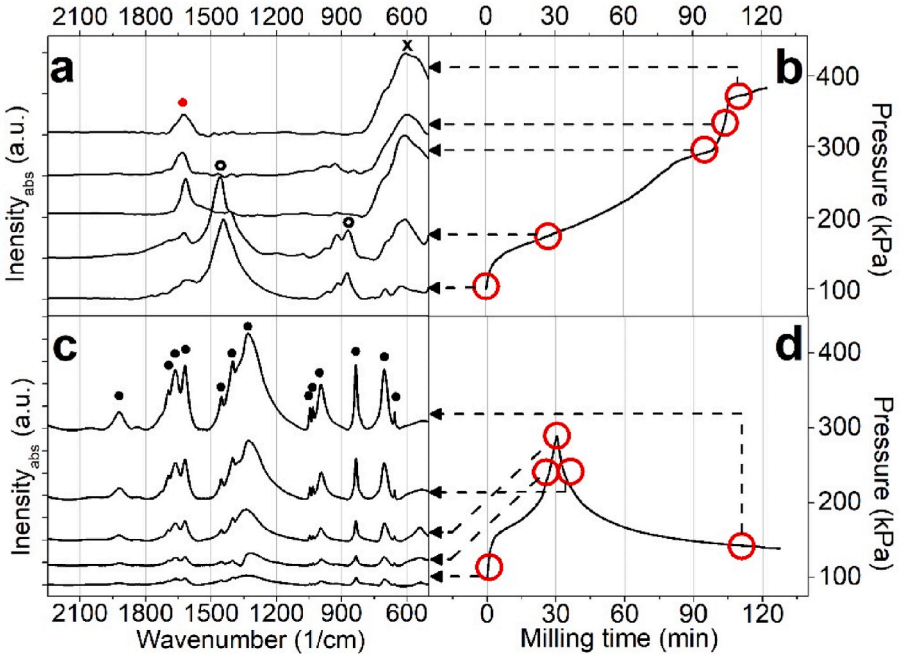

Fig. 6. FT-IR spectra and GTM curves of samples A (a, b) and K (c, d), recorded at different times during milling. Sampling points marked as red circles on GTM curves (x, SnO; o, Na_2CO_3; •, H_2O; •, $NaHCO_3$).

the aqueous direction (Eq. (6)).

$$CO_{2(g)} \leftrightarrow CO_{2(aq)} \tag{6}$$

The solubility of CO_2 is increased by its reaction with H_2O to form HCO_3^- and H^+ ions (Eq. (7)).

$$CO_{2(aq)} + H_2O \leftrightarrow HCO^-_{3(aq)} + H^+_{(aq)} \tag{7}$$

As solid Na_2CO_3 is present, it shifts the balance between dissolved CO_2 and HCO_3^- and CO_3^{2-} ions (Eqs (8) and (9)).

$$Na_2CO_{3(s)} \leftrightarrow 2Na^+_{(aq)} + CO^{2-}_{3(aq)} \tag{8}$$

$$CO^{2-}_{3(aq)} + H^+_{(aq)} \leftrightarrow HCO^-_{3(aq)} \tag{9}$$

Finally, HCO_3^- and Na^+ ions formed during the process (Eqs (7)–(9)) are converted to $NaHCO_3$ (Eq. (10)).

$$2HCO^-_{3(aq)} + 2Na^+_{(aq)} \leftrightarrow 2NaHCO_{3(aq)} \tag{10}$$

4. Conclusions

The appearance of unexpected pressure peaks was governed by the interaction between CO_2 formation according to Eq. (1) and CO_2 consumption according to Eq. (4). The Na_2CO_3 was consumed in both reactions, whereas $NaHCO_3$ formed only in the second. The $NaHCO_3$ could react with the remaining $SnCl_2$ to release previously stored CO_2. The availability of Na_2CO_3 depended on the composition of the reactant mixture (Table 2). In quasi-stoichiometric compositions, CO_2 formation and $NaHCO_3$ decomposition were balanced, the pressure rose steadily, and the pressure peak is was pronounced. Increasing the Na_2CO_3 excess enabled the capture of increasing amounts of CO_2 up to the point of 100% excess (sample K) when all CO_2 was re-captured in the form of $NaHCO_3$. At this point, the pressure was rather similar to the starting value whereas $SnCl_2$ conversion was complete. This clearly underlines the limitations of pressure-derived conversion calculations similar to Eq. (3).

Even though our primary goal was explaining the anomalous pressure evolution to assist the mechanochemistry community in the correct interpretation of experimental data, CO_2 capture with Na_2CO_3 is also an existing industrial technology, especially for treatment of flue gases. Wang et al. found that hydrated Na_2CO_3 powders with 30 wt % water content can achieve a CO_2 sorption capacity of 282 mg/g within 60 min and fast CO_2 uptake [44]. In our case, 415 mg/g CO_2 sorption capacity was achieved with only 3.28 wt % water. With the right parameters this takes less than 60 min, and the reaction time can be reduced further by increasing the rotational speed or the number of milling balls. Peruzzini et al. performed CO_2 capture by aqueous (0.83 mol/dm^3) Na_2CO_3 and this system operated at almost 80% efficiency [45]. McMichael et al., similarly to our case, conducted experiments on CO_2 capture under dry conditions and found that it was effective in the temperature range of 60–70 °C and capture of up to 90% of the CO_2 was possible at appropriate reaction conditions [46]. These data are very consistent with our results; in our case the heat released during milling provided the required temperature.

Thus, in addition to identifying the processes that affect pressure during carbonate-based mechanochemical metal oxide formation, an efficient carbon sequestration process was also found.

Author contributions

Gábor Kozma: Conceptualization, Methodology, Formal analysis, Visualization, Validation, Writing – original draft. *Andrea Rónavári:* Investigation, Writing – review & editing. *Zoltán Kónya:* Supervision, Funding acquisition. *Ákos Kukovecz:* Conceptualization, Supervision, Funding acquisition, Writing – review & editing.

Declaration of competing interest

The authors declare that they have no known competing financial interests or personal relationships that could have appeared to influence the work reported in this paper.

Acknowledgements

The work was supported by the János Bolyai Research Fellowship of the Hungarian Academy of Sciences BO/00835/19/7 and by the professional support of the New National Excellence Program of the Ministry of Innovation and Technology UNKP-21-5-SZTE-547. Project no. TKP2021-NVA-19 has been implemented with support provided by the Ministry of Innovation and Technology of Hungary from the National Research, Development and Innovation Fund, financed under the TKP2021-NVA funding scheme.

References

[1] P. Baláž, M. Achimovičová, M. Baláž, P. Billik, Z. Cherkezova-Zheleva, J.M. Criado, F. Delogu, E. Dutková, E. Gaffet, F.J. Gotor, R. Kumar, I. Mitov, T. Rojac, M. Senna, A. Streletskii, K. Wieczorek-Ciurowa, Hallmarks of mechanochemistry: from nanoparticles to technology, Chem. Soc. Rev. 42 (2013) 7571–7637.
[2] S.L. James, C.J. Adams, C. Bolm, D. Braga, P. Collier, T. Friščić, F. Grepioni, K.D. M. Harris, G. Hyett, W. Jones, A. Krebs, J. Mack, L. Maini, A.G. Orpen, I.P. Parkin, W.C. Shearouse, J.W. Steed, D.C. Waddell, Mechanochemistry: opportunities for new and cleaner synthesis, Chem. Soc. Rev. 41 (2012) 413–447.
[3] M. Zhang, H. Yang, D. Li, L. Ma, Y. Lin, Giant energy storage efficiency and high recoverable energy storage density achieved in K0.5Na0.5NbO3-Bi(Zn0.5Zr0.5)O3 ceramics, J. Mater. Chem. C 8 (2020) 8777–8785.
[4] F. Yan, H. Bai, X. Zhou, G. Ge, G. Li, B. Shen, J. Zhai, Realizing superior energy storage properties in lead-free ceramics via a macro-structure design strategy, J. Mater. Chem. 8 (2020) 11656–11664.
[5] S. Intasa-ard, K. Imwiset, S. Bureekaew, M. Ogawa, Mechanochemical methods for the preparation of intercalation compounds, from intercalation to the formation of layered double hydroxides, Dalton Trans. 47 (2018) 2896–2916.
[6] A. Dodd, A. McKinley, M. Saunders, T. Tsuzuki, Mechanochemical synthesis of nanocrystalline SnO2-ZnO photocatalysts, Nanotechnology 17 (2006) 692–698.
[7] N.J. Tharayil, R. Raveedran, A.V. Vaidyan, Synthesis and characterization of nanosized cobalt-manganese spinel oxide, Indian J. Pure Appl. Phys. 46 (2008) 47–53.
[8] M.H. Chang, H.S. Liu, C.Y. Tai, Preparation of copper oxide nanoparticles and its application in nanofluid, Powder Technol. 207 (2011) 378–386.
[9] M.E. Casco, S. Kirchhoff, D. Leistenschneider, M. Rauche, E. Brunner, L. Borchardt, Mechanochemical synthesis of N-doped porous carbon at room temperature, Nanoscale 11 (2019) 4712–4718.
[10] F.J. Castro, V. Fuster, G. Urretavizcaya, MgH2 synthesis during reactive mechanical alloying studied by in-situ pressure monitoring, Int. J. Hydrogen Energy 37 (2012) 16844–16851.
[11] S. Doppiu, L. Schultz, O. Gutfleisch, In situ pressure and temperature monitoring during the conversion of Mg into MgH2 by high-pressure reactive ball milling, J. Alloys Compd. 427 (2007) 204–208.
[12] M. Gheisari, M. Mozaffari, M. Acet, J. Amighian, Preparation and investigation of magnetic properties of wustite nanoparticles, J. Magn. Magn Mater. 320 (2008) 2618–2621.
[13] A. Hasanpour, M. Mozaffari, J. Amighian, Preparation of Bi-Fe3O4 nanocomposite through reduction of Bi2O3 with Fe via high-energy ball milling, Phys. B Condens. Matter 387 (2007) 298–301.
[14] S. Coste, G. Bertrand, C. Coddet, E. Gaffet, H. Hahn, H. Sieger, High-energy ball milling of Al2O3-TiO2 powders, J. Alloys Compd. 434 (2007) 489–492.
[15] K. Wieczorek-Ciurowa, D. Oleszak, K. Gamrat, Mechanosynthesis and process characterization of some nanostructured intermetallics-ceramics composites, J. Alloys Compd. 434 (2007) 501–504.
[16] M.P. Fernandez-Garcia, J.M. Teixeira, P. Machado, M.E. Leblebici, J.C.B. Lopes, C. Freire, J.P. Araujo, Monitoring in real time the production of Fe-oxide nanoparticles, Chem. Eng. Sci. 138 (2015) 600–606.
[17] A.V. Ghule, K. Ghule, T. Punde, J.Y. Liu, S.H. Tzing, J.Y. Chang, H. Chang, Y. C. Ling, In situ monitoring of NiO-Al2O3 nanoparticles synthesis by thermo-Raman spectroscopy, Mater. Chem. Phys. 119 (2010) 86–92.
[18] B.M. Concha, M. Chatenet, C. Coutanceau, F. Hahn, In situ infrared (FTIR) study of the borohydride oxidation reaction, Electrochem. Commun. 11 (2009) 223–226.
[19] S.H. Nahm, Use of dielectric spectroscopy for real-time in-situ reaction monitoring, Jct Res. 3 (2006) 257–265.
[20] L.N. Warr, H. Hofmann, In situ monitoring of powder reactions in percolating solution by wet-cell X-ray diffraction techniques, J. Appl. Crystallogr. 36 (2003) 948–949.
[21] A. Sekiguchi, Y. Miyake, M. Isono, Analysis of deprotection reaction in chemically amplified resists using an Fourier transform infrared spectrometer with an exposure tool, Jpn. J. Appl. Phys. Part 1-Regular Pap. Short Notes Rev. Pap. 39 (2000) 1392–1398.

[22] M. Baláž, A. Zorkovská, F. Urakaev, P. Baláž, J. Briančin, Z. Bujňáková, M. Achimovičová, E. Gock, Ultrafast mechanochemical synthesis of copper sulfides, RSC Adv. 6 (2016) 87836–87842.
[23] R. Scholl, R. Wegerle, W. Mutter, Gas pressure and temperature measuring system (GTM) for in-situ data acquisition during planetary ball milling, in: J. Eckert, H. Schlorb, L. Schultz (Eds.), Metastable, Mechanically Alloyed and Nanocrystalline Materials, 2000, pp. 964–972. Pts 1 and 2.
[24] Y. Li, J.-G. Wang, W. Hua, H. Liu, B. Wei, Heterostructured Sn/SnO2−x nanotube peapods with a strong plasmonic effect for photoelectrochemical water oxidation, J. Mater. Chem. 7 (2019) 16883–16891.
[25] L. Zhang, H. Zhang, H. Huang, Y. Liu, Z. Kang, Ag3PO4/SnO2 semiconductor nanocomposites with enhanced photocatalytic activity and stability, New J. Chem. 36 (2012) 1541–1544.
[26] M. Periyasamy, A. Kar, Modulating the properties of SnO2 nanocrystals: morphological effects on structural, photoluminescence, photocatalytic, electrochemical and gas sensing properties, J. Mater. Chem. C 8 (2020) 4604–4635.
[27] K. Xu, S. Tian, J. Zhu, Y. Yang, J. Shi, T. Yu, C. Yuan, High selectivity of sulfur-doped SnO2 in NO2 detection at lower operating temperatures, Nanoscale 10 (2018) 20761–20771.
[28] F.C. Yang, Z.G. Guo, Tuning SnO2 architectures with unitary or composite microstructure for the application of gas sensors, J. Colloid Interface Sci. 462 (2016) 140–147.
[29] Y. Lin, C. Li, W. Wei, Y. Li, S. Wen, D. Sun, Y. Chen, S. Ruan, A new type of acetylene gas sensor based on a hollow heterostructure, RSC Adv. 5 (2015) 61521–61527.
[30] S.M. Jung, D.W. Kim, H.Y. Jung, Unconventional capacity increase kinetics of a chemically engineered SnO2 aerogel anode for long-term stable lithium-ion batteries, J. Mater. Chem. 8 (2020) 8244–8254.
[31] H. Qiu, L. Zhao, M. Asif, X. Huang, T. Tang, W. Li, T. Zhang, T. Shen, Y. Hou, SnO2 nanoparticles anchored on carbon foam as a freestanding anode for high performance potassium-ion batteries, Energy Environ. Sci. 13 (2020) 571–578.
[32] W. Chen, K. Song, L. Mi, X. Feng, J. Zhang, S. Cui, C. Liu, Synergistic effect induced ultrafine SnO2/graphene nanocomposite as an advanced lithium/sodium-ion batteries anode, J. Mater. Chem. 5 (2017) 10027–10038.
[33] M. Zhang, F. Wu, D. Chi, K. Shi, S. Huang, High-efficiency perovskite solar cells with poly(vinylpyrrolidone)-doped SnO2 as an electron transport layer, Mater. Adv. 1 (2020) 617–624.
[34] H. Guo, Z. Chen, X. Wang, Q. Cang, C. Ma, X. Jia, N. Yuan, J. Ding, Significant increase in efficiency and limited toxicity of a solar cell based on Sb2Se3 with SnO2 as a buffer layer, J. Mater. Chem. C 7 (2019) 14350–14356.
[35] Q. Wali, A. Fakharuddin, R. Jose, Tin oxide as a photoanode for dye-sensitised solar cells: current progress and future challenges, J. Power Sources 293 (2015) 1039–1052.
[36] N. Zhou, L. Polavarapu, Q. Wang, Q.H. Xu, Mesoporous SnO2-coated metal nanoparticles with enhanced catalytic efficiency, ACS Appl. Mater. Interfaces 7 (2015) 4844–4850.
[37] J. Yu, D. Zhao, X.L. Xu, X. Wang, N. Zhang, Study on RuO2/SnO2: novel and active catalysts for CO and CH4 oxidation, ChemCatChem 4 (2012) 1122–1132.
[38] P.W. Park, H.H. Kung, D.W. Kim, M.C. Kung, Characterization of SnO2/Al2O3 lean NOx catalysts, J. Catal. 184 (1999) 440–454.
[39] L.M. Cukrov, T. Tsuzuki, P.G. McCormick, SnO2 nanoparticles prepared by mechanochemical processing, Scripta Mater. 44 (2001) 1787–1790.
[40] F. Legendre, S. Poissonnet, P. Bonnaillie, Synthesis of nanostructured SnO2 materials by reactive ball-milling, J. Alloys Compd. 434 (2007) 400–404.
[41] G. Kozma, A. Kukovecz, Z. Konya, Spectroscopic studies on the formation kinetics of SnO2 nanoparticles synthesized in a planetary ball mill, J. Mol. Struct. 834 (2007) 430–434.
[42] Y.X. Li, W.F. Chen, X.Z. Zhou, Z.Y. Gu, C.M. Chen, Synthesis of CeO2 nanoparticles by mechanochemical processing and the inhibiting action of NaCl on particle agglomeration, Mater. Lett. 59 (2005) 48–52.
[43] E.N. Ramsden, Chemistry of the Environment, Stanley Thornes, 1996.
[44] Y. Cai, W. Wang, L. Li, Z. Wang, S. Wang, H. Ding, Z. Zhang, L. Sun, W. Wang, Effective capture of carbon dioxide using hydrated sodium carbonate powders, Materials 11 (2018) 183.
[45] F. Barzagli, C. Giorgi, F. Mani, M. Peruzzini, CO2 capture by aqueous Na2CO3 integrated with high-quality CaCO3 formation and pure CO2 release at room conditions, J. CO2 Util. 22 (2017) 346–354.
[46] Y. Liang, D.P. Harrison, R.P. Gupta, D.A. Green, W.J. McMichael, Carbon dioxide capture using dry sodium-based sorbents, Energy Fuels 18 (2004) 569–575.